Measurement 154 (2020) 107494

Contents lists available at ScienceDirect

Measurement

journal homepage: www.elsevier.com/locate/measurement

Interpolation methods in GPR tomographic imaging of linear and volume anomalies for cultural heritage diagnostics

Magdalena Rucka [a,*], Erwin Wojtczak [a], Monika Zielińska [b]

[a] Department of Mechanics of Materials and Structures, Faculty of Civil and Environmental Engineering, Gdańsk University of Technology, Narutowicza 11/12, 80-233 Gdańsk, Poland
[b] Department of Technical Fundamentals of Architectural Design, Faculty of Architecture, Gdańsk University of Technology, Narutowicza 11/12, 80-233 Gdańsk, Poland

ARTICLE INFO

Article history:
Received 26 September 2019
Received in revised form 11 December 2019
Accepted 8 January 2020
Available online 13 January 2020

Keywords:
Ground penetrating radar
Non-destructive testing
Time slice
Interpolation technique
Historical building

ABSTRACT

This paper presents results of a ground penetrating radar (GPR) survey conducted in St. Joseph's Church in Gdańsk, Poland. The aim of the study was to produce tomographic imaging of a renovated floor as well as the objects buried under the floor to detect linear and volume inclusions. The assumed track spacing was meaningfully greater than the single signal spacing in each track, which induced the need for interpolation methods to estimate signal values in the areas beyond the trace lines. Various interpolation techniques were used to prepare the tomography maps. GPR time slices allowed the identification of reinforcing meshes, underfloor heating system elements and the foundations of entrances to crypts. The results obtained were compared to the exact images acquired in a dense regular grid to evaluate the efficiency of the applied interpolation methods and to verify the possibility of conducting GPR surveys with coarse track spacing.

1. Introduction

Imaging of the internal structure of building objects is one of the most challenging tasks in modern non-destructive testing (NDT). This issue is particularly important for cultural heritage structures, especially before an intervention, to assess the general condition of an object, or after renovation, to evaluate the effectiveness of the conducted repairs. Techniques for imaging structural elements, which allows the user to observe voids, moisture flow or heat transport [1–3], as well as identify the mechanical, physical and chemical characteristics of materials [4–7], constitute the main components involved in conservation and restoration of historical monuments.

Among various non-destructive methods, mechanical and electromagnetic wave propagation techniques are of great importance to structural imaging [8]. In general, two main approaches allow a precise diagnosis. The first approach is computed tomography, which refers to the cross-sectional imaging of an object from a set of projections that pass through it in many different directions and is performed by solving inverse problems [9]. Both ultrasound and microwave tomography have been widely used for the inspection of concrete and masonry objects. Binda et al. [10] evaluated stone piers of the Notho Cathedral using sonic and radar tomographic imaging. Pérez-Gracia et al. [11] reconstructed the velocity distribution in columns of the Mallorca Cathedral using ultrasonic tomography. Zendri et al. [12] investigated historical columns with ultrasonic tomography before and after consolidation interventions. Zielińska and Rucka [13] applied ultrasonic waves and tomographic imaging to assess the condition of the adhesive connection between a steel reinforcing bar embedded inside pillars and the surrounding pillar body. Shiotani et al. [14] examined a deteriorated pier in a concrete dam. They used ultrasonic transmission tomography to evaluate the repair effect before and after grouting. They examined a sample before the repair process and after it, considering both the fresh and hardened grout. Chai et al. [15] used travel time ultrasonic tomography to detect unfilled tendon ducts and honeycomb defects in concrete specimens. Haach and Ramirez [16] analysed the influence of different discontinuities and different arrangements of transducers on the tomograms of concrete prisms.

The second approach is the construction of tomographic images as time or depth slices (so called C-scans), which represent cross-sections of an investigated object at a certain depth. Such an approach requires one-sided measurements of wave propagation conducted in a dense grid over the entire tested area; this approach is very popular for testing floors, slabs or underground objects. Many examples of the successful application of time slices for detecting defects or internal inclusions can be found in literature. Drobiec, Jasiński, and Mazur [17] analysed the possibility of

* Corresponding author.
E-mail address: magdalena.rucka@pg.edu.pl (M. Rucka).

https://doi.org/10.1016/j.measurement.2020.107494
0263-2241/

Fig. 1. Photograph of the floor in St. Joseph's Church in Gdańsk, Poland (Google Maps coordinates in a WGS84 system: 54.354111 N, 18.647135 E): a) excavation view, b) concreting of the reinforced concrete slab, c), d) floor heating view with marked locations of the entrances to the crypts.

detecting closely spaced rebars in concrete specimens based on ground penetrating radar (GPR) time slices. Ultrasonic time slices were used by Schabowicz [18] to evaluate the condition of a foundation slab. During tests, a tomograph antenna was shifted by a distance of 0.10 m, resulting in approximately 240 time signals along each of the traces. Neubauer et al. [19] collected GPR data in a regular grid and visualised time-slices for archaeological applications. They analysed different raster sizes (from 5 cm × 0.5 m to 20 cm × 2 m) and different directions of measurements.

There are two opposite requirements for creating tomographic images. As the grid density increases, the map resolution also increases, but the field effort significantly increases. However, measurement over a sparse grid is relatively fast, but the inspection results suffer from poor resolution and a possible omission of small anomalies. Therefore, interpolation and averaging techniques play crucial role in the construction of GPR C-scans. Goodman, Nishimura, and Rogers [20] developed GPR time slices from closely spaced parallel profiles collected along one direction at archaeological sites. A-scans (single waveforms plotted as a function of time) were collected in a 1 m grid and then spatially averaged from surrounding points with a search radius of 2.2 m. Orlando [21] performed a georadar survey over an archaeological settlement. The GPR data were registered in both directions, on a grid of 0.5 m × 1.0 m. Then, the profiles were spatially resampled by inserting the interpolated traces, resulting in regular grid of a size 0.1 m × 0.1 m. De Donno, Di Giambattista, and Orlando [22] used GPR imaging to characterise reinforced masonry samples, before and after the application of a load. GPR data, acquired along profiles spaced 0.1 m apart and interpolated in both directions to obtain time slices, were compared with electrical resistivity tomography. Samet et al. [23] used interpolation techniques to determine the optimal profile interval. They collected profiles in one direction over an underground structure and interpolated them in both the horizontal and vertical direction on a regular mesh. Klęsk, Kapruziak, and Olech [24] focused on using GPR to detect antitank mines composed of different materials (plastic and metallic). They proposed a calculation for multiple integral images to reduce the time cost of the signal processing. In each case, the data was registered over an area of 1 m^2 and the scan resolution was assumed to be 1 cm in both directions. Zhao et al. [25] performed GPR scans along one direction at the profile spacing of 1.0 m and 0.5 m. Then, they proposed energy and similarity slices to image and characterise an archaeological site to detect buried objects.

Existing papers have presented applications of interpolation methods to detect buried objects, mainly archaeological structures, and have indicated that interpolation of GPR data has a significant impact on the C-scans. The motivation of this work was to investigate how different methods of interpolation influenced the possibility of imaging embedded objects of various shapes. In this paper, we examine tomographic images of the internal structure of a historical floor that contains some modern elements inserted during renovation, as well as buried structures under the floor. In the GPR surveys, the assumed profile interval was meaningfully greater than the trace interval, which induced the need for interpolation methods to estimate signal values in the areas beyond the trace lines. The main aim of this study is to evaluate the possibility of detection of linear (reinforcing meshes, underfloor heating system elements) and volume (foundations of entrances to crypts) anomalies in the GPR time slices. Calculations with simple linear, bilinear and inverse distance weighting interpolation techniques were conducted to prepare the visualizations. The results obtained

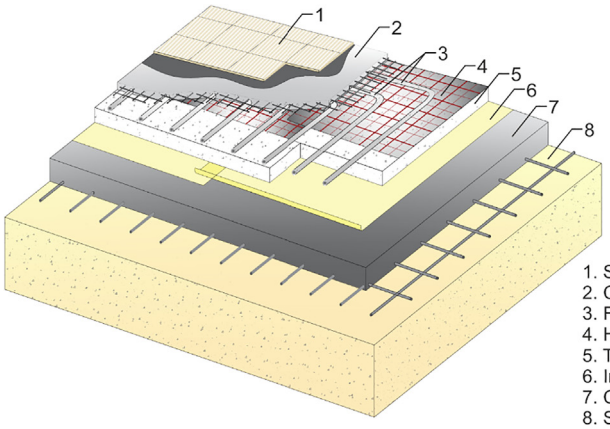

1. Stone tiles with adhesive (3 cm thick)
2. Concrete screed (5 cm thick) reinforced with steel mesh
3. Floor heating cables (PE-AL-PE pipes)
4. Heat reflective aluminum sheet
5. Thermal insulation (10 cm thick polystyrene)
6. Insulation foil
7. Cross-reinforced concrete slab (15 cm thick)
8. Sand backfill on a geotextile

Fig. 2. Cross-section of new floor in St. Joseph's Church with a description of the layers.

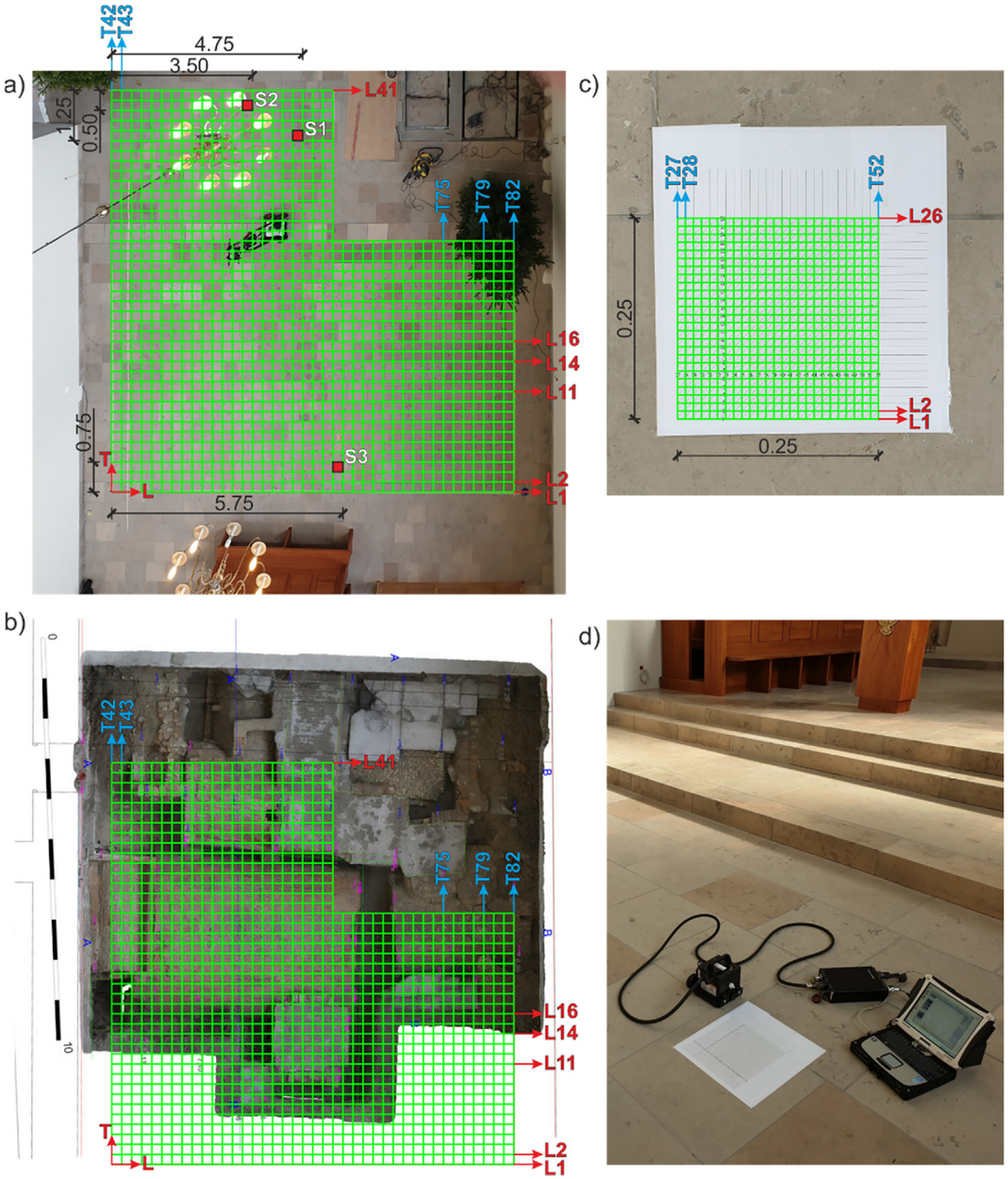

Fig. 3. The floor of St. Joseph's Church (dimensions in m) investigated in this paper: a) GPR survey area on the part of floor that was investigated, with the three selected squares indicated (S1, S2, S3), b) grid of GPR profiles superimposed on the excavation view, c) GPR traces on a specific square, d) GPR equipment.

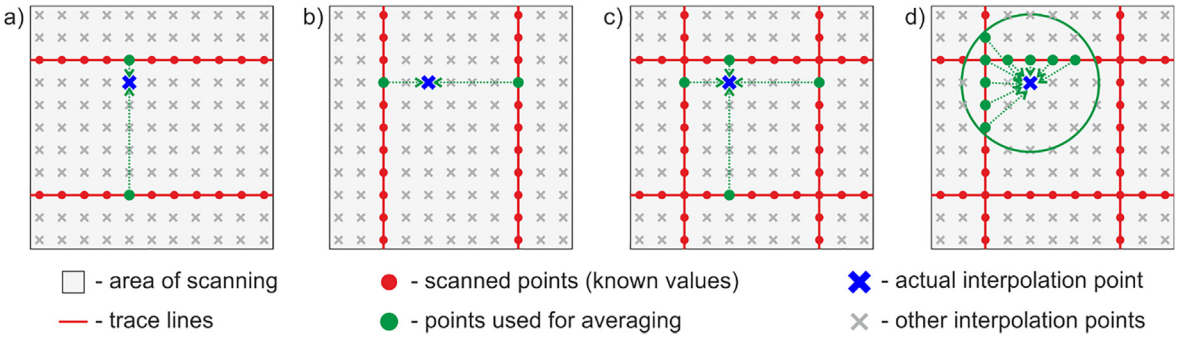

Fig. 4. Interpolation algorithms: a), b) simple linear interpolation with longitudinal and transverse scans, respectively, c) bilinear interpolation, d) inverse distance weighting (IDW) technique.

were compared to the exact images acquired over a dense regular grid to evaluate the efficiency of the applied interpolation methods.

2. Materials and methods

2.1. Object of investigations

GPR measurements were conducted in St. Joseph's Church in Gdańsk, Poland (Google Maps coordinates in a WGS84 system: 54.354111 N, 18.647135 E). This historical building from the 15th century underwent a major renovation in 2017–2019, including the renovation of the floor (Fig. 1). During the renovation in the main hall of the church, brick crypts, dating to the 17th and 18th centuries, were discovered. The crypts contain human remains and coffins and were located several dozen centimetres below the floor. Excavations were conducted only within the part of the floor located directly next to the chancel (Fig. 1a).

After the archaeological research, the crypts were sealed and covered with sand backfill on a geotextile. Entrances to the crypts were kept in designated places (Fig. 1c–d). Fig. 2 shows the floor layers constructed during the renovation. A cross-reinforced

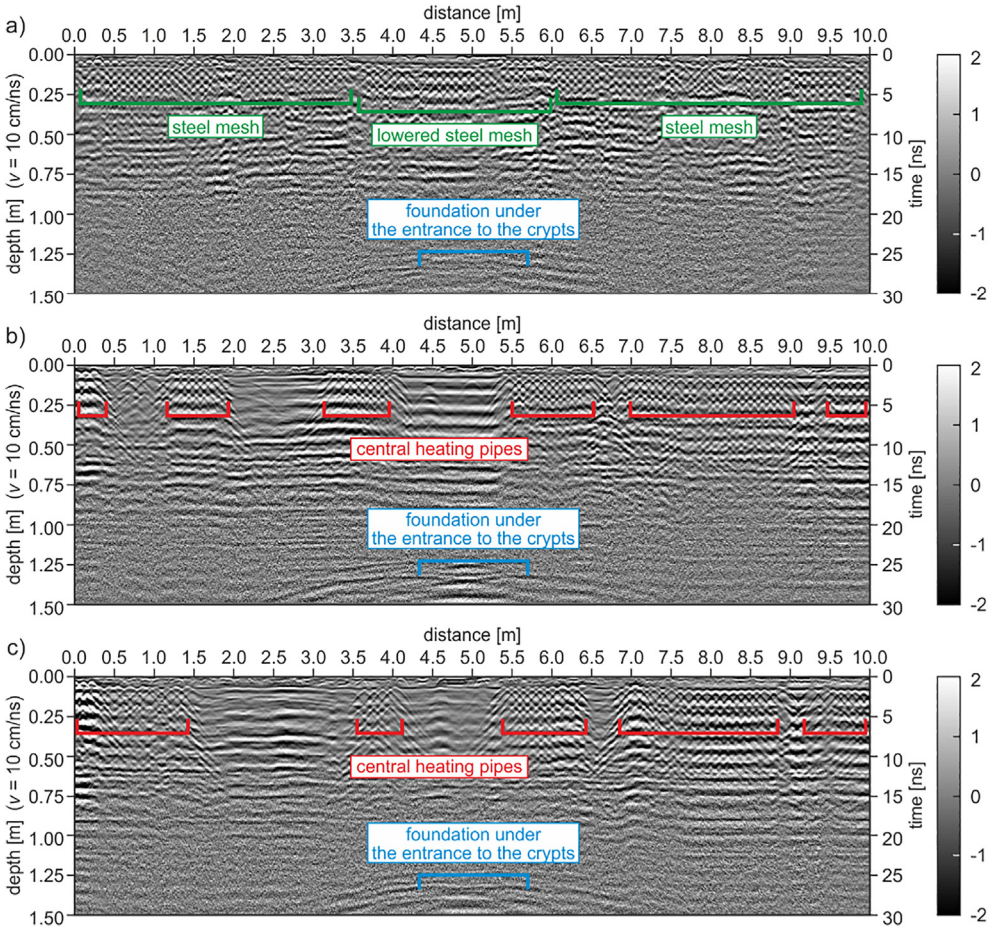

Fig. 5. Longitudinal GPR radargrams (values in V): a) scan L11; b) scan L14; c) scan L16.

concrete slab with a 10 × 10 cm mesh composed of 12 mm steel rods was implemented on the prepared subsoil (Fig. 1b). The meshes were concentrated in the locations of the previous excavations. An insulation foil and a 10 cm thick polystyrene layer were laid on the concrete plate. The thermal insulation was covered with a heat reflective aluminium sheet to enforce reflection of heat energy, limiting its loss. Floor heating, made of layered pipes with diameters of 16 mm, was encased in the concrete screed. Polyethylene forms the inner and outer layers, between which a welded aluminium layer was inserted. The concrete screed was reinforced with a mesh composed of welded, overlapping steel bars. The top floor layer was made of stone tiles measuring 50 × 50 cm.

2.2. Data acquisition and equipment

The inspection was conducted on the part of the floor indicated in Fig. 3a. The top right corner was omitted in the GPR scan because it was inaccessible due to the renovation conducted during measurements. The survey area was chosen to cover the excavated fragments of the floor (Fig. 3b). The experiment was conducted in two stages. In stage #1, 41 longitudinal profiles (L1 to L41) and 41 transverse profiles (T42 to T82) were traced (Fig. 3a and b) with a distance of 25 cm, and GPR measurements were conducted along these traces. These profiles divided the scan area into 1330 sub-areas, i.e., squares with a side length of 25 cm. In stage #2, measurements of the selected sub-areas were performed with denser profiling. Three squares (denoted as S1, S2 and S3 in Fig. 3a) were selected for precise tomographic imaging. The distance between particular profiles in stage #2 decreased to 1 cm. Fig. 3c shows square S1 during measurements. The grid printed on a paper stuck on the floor surface enabled the scans to be performed at a constant distance.

The GPR surveys were conducted using the Aladdin system (Fig. 3d), which is manufactured by IDS GeoRadar (Pisa, Italy) and equipped with an antenna unit operating with a central frequency of 2 GHz. The dimensions of the antenna were 12 cm × 12 cm. The registered time range was 32 ns and the number of captured samples was 1024. A step distance between particular A-scans was set to be 1 cm. The radargrams were collected using K2 FastWave software and then processed in GRED HD software using automatic time zero correction, bandpass filtration (500–3000 MHz) and smoothed gain. Finally, GPR data were analysed using scripts developed in the MATLAB® environment.

2.3. Techniques of GPR image construction

In two-direction GPR profiling, if the A-scan spacing in an individual GPR profile is finer than the distance between the particular profiles, the tomographic imaging requires additional signal processing. Interpolation techniques are needed to calculate values of the points beyond the trace lines. Two essential issues need to be considered: the selection rule for the points and a technique for averaging the values of the chosen points. If the GPR survey involves a single-dimensional scanning, a common methodology is the typical simple linear interpolation technique. This technique requires calculating a weighted arithmetic mean of known values in the points that are rectangular projections of an interpolated point on two adjacent trace lines (Fig. 4a, b, longitudinal and transverse scanning, respectively). A dataset for each interpolation point contains only two values. The method is useful especially when searching for linear anomalies perpendicular to the scan direction,

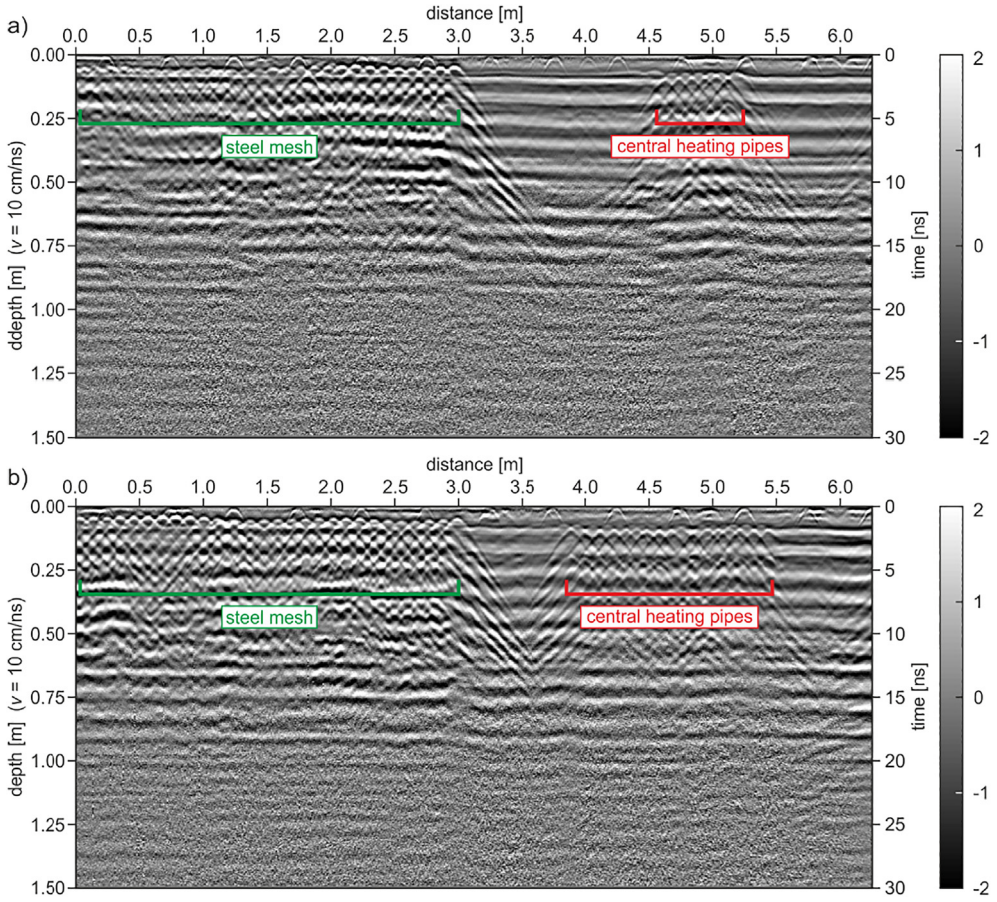

Fig. 6. Transverse GPR radargrams (values in V): a) scan T75; b) scan T79.

e.g. one direction reinforcement in concrete structures. To improve the quality of the GPR time slices, two-dimensional scanning can be performed, which provides more accurate data. In this case, a bilinear interpolation (Fig. 4c) can be conducted for each point. Bilinear interpolation is defined as a combination of two independent linear interpolations in both directions. The final value is an arithmetic mean of the values obtained from interpolation in both the transverse and longitudinal directions. In this case, four points are used for the calculations (two from the longitudinal and two from the transverse scans). Such an approach can be efficient for linear anomalies that are oriented in two directions, e.g., reinforcing meshes.

Another simple approach from a group of spatial interpolation methods, is the inverse distance weighting (IDW) technique, which is especially applicable for scattered data [26]. This technique is one of the common deterministic methods for multivariate interpolation with many applications, e.g., in meteorology [27], hydrology [28], image analysis [29] or GPR tomographic imaging [30]. The interpolated value is calculated by averaging a set of values v_i from specific points using the weighted arithmetic mean, as follows:

$$v_{int} = \frac{\sum_{i=1}^{N} w_i v_i}{\sum_{i=1}^{N} w_i} \tag{1}$$

where the weighting factors w_i are calculated based on the distances d_i between the interpolated point and each point from the dataset in consideration, as follows:

$$w_i = \frac{1}{d_i^s} \tag{2}$$

where s is an inverse exponential factor, also called the smoothing factor. If $s = 1$, the weighting factor is inversely proportional to the distance. For higher s values, the influence of nearby points is much stronger than that of further ones. The smoothing factor is usually assumed to be equal to 2. The key issue is the appropriate choice of points for interpolation. In general, the points in the whole dataset can participate in the calculation for each unknown value; however, such an approach is time-consuming. A solution to this problem is to exclude points that are distant from each interpolated point, because less importance is assigned to them in IDW. One of the methods (Fig. 4d) involves searching for scanned points in the area designated by a circle with a specific radius centred on the interpolated point [30,31]. To obtain the tomography in the entire analysed area, the circle diameter needs to be at least equal to the distance between two adjacent scans. Otherwise, several points will have an empty dataset for interpolation, resulting in an incomplete tomographic image. The IDW method can be successfully applied to search for volume anomalies. Both simple linear interpolation and bilinear interpolation are examples of IDW applied to degenerated datasets for $s = 1$.

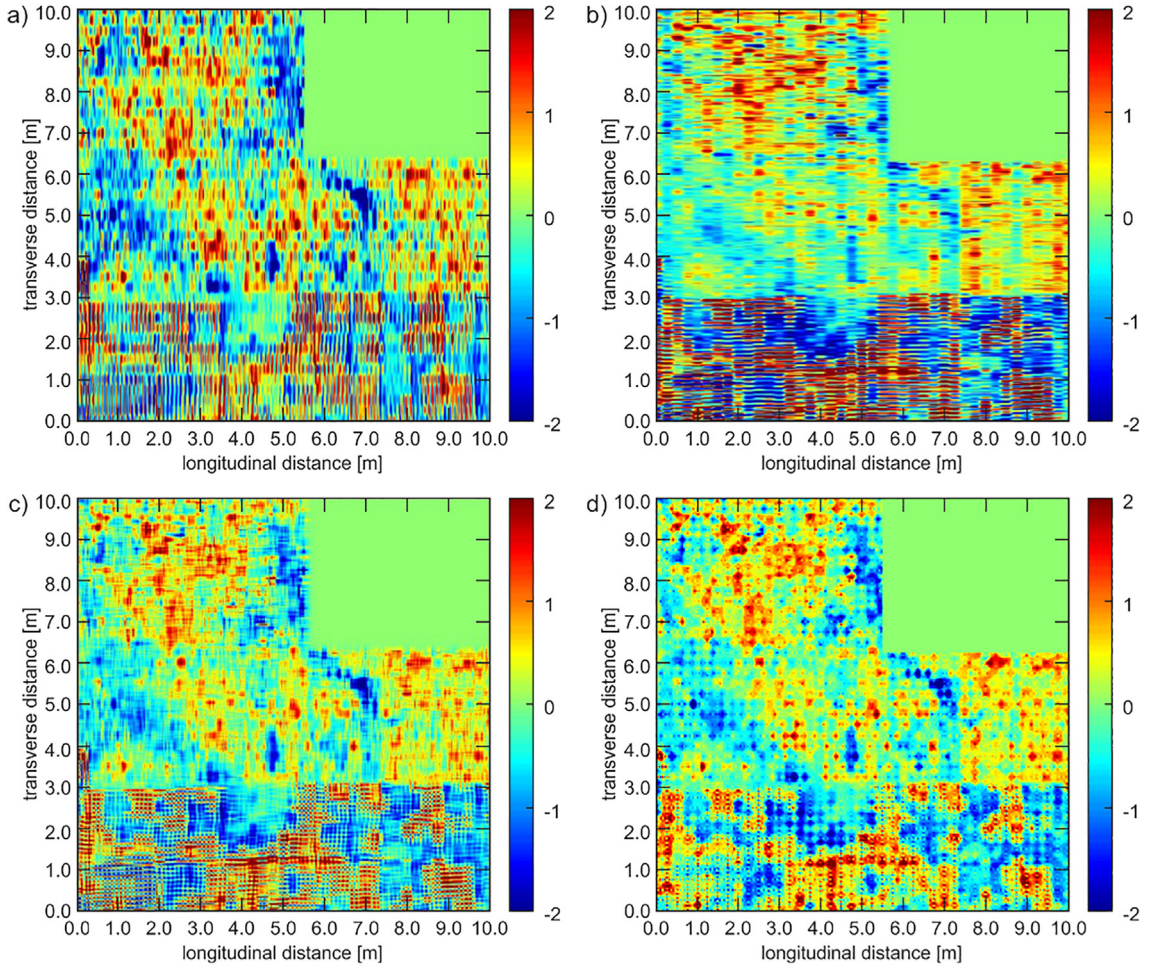

Fig. 7. GPR tomography maps for a depth of 4.6875 cm (values in V): a) simple linear interpolation using longitudinal (L) scans, b) simple linear interpolation using transverse (T) scans, c) bilinear interpolation, d) IDW interpolation with a radius of 13 cm.

3. Results and discussion

3.1. GPR surveys of floor

Figs. 5 and 6 present the B-scans (radargrams) prepared based on the longitudinal (L) and transverse (T) measurements of the tested part of the floor, respectively. The effective depth of penetration for the GPR system used was 1.5 m. Due to the complexity of the analysed medium (cf. Fig. 2), the electromagnetic wave propagation velocity was assumed to be approximately 10 cm/ns based on a diffraction hyperbola in the concrete layer.

Three longitudinal (L11, L14 and L16) and two transverse radargrams (T75 and T79) are described below. The L11 (Fig. 5a) profile ran through both of these radargrams in the excavated and non-excavated parts of the floor (see Fig. 3b). Numerous hyperbolic patterns were visible in the radargram, which reveals the existence of bars of steel mesh embedded in the concrete screed. Any reflections from the heating system were not noticeable because they were masked by reflections from the reinforcement mesh above them. In the area of the entrance to the crypts, which was located approximately between 3.5 m and 6.0 m depth, the reinforcement mesh was identified at a lower depth, probably due to the lack of central heating in this area. The radargram obtained along profile L14 is displayed in Fig. 5b. The part of the scan that passed over the excavations extends from the beginning of the radargram for a length of 7.0 m (see Fig. 3b). The central heating pipes were arranged in loops. The radargrams alternately present their course in positions parallel and perpendicular the measured path. The pipes that run perpendicular generated distinguishable reflections. These features are visible in sections 0 – 0.4 m, 1.2 – 1.8 m, 3.1 – 3.9 m, 5.5 – 6.5 m, 7.0 – 9.0 m and 9.5 – 10.0 m. The pipes running in parallel were not possible to identify on the radargrams. Aluminium foil, which was laid under the floor heating, also resulted in multiple reflections of electromagnetic waves under the upper row of hyperbolas, masking any potential reflections below it. The reinforcement of the concrete screed was not observed in this radargram. The L16 (Fig. 5c) scan was conducted on the floor only in the excavated area. Like in the L14 scan, only the reflections from the floor heating pipes were visible in several specific areas and no screed reinforcement was observed. Additionally, all analysed radargrams (L11, L14 and L16) revealed a reflection at a depth of approximately 1.30–1.40 m. These reflections may prove the existence of some kind of the foundation under the entrance to the crypts.

Two transverse radargrams (T75 and T79) crossed both the excavated and non-excavated parts of the floor. In both scans, a clear boundary between these parts can be observed, at a distance of approximately 3.0 m from the beginning of the scan (Fig. 6). Wave reflections from the reinforcing mesh are clearly visible in this area. Further parts of the radargrams (4.5–5.2 m in T75 and 3.8–5.5 m in T79) shows reflections from the underfloor heating pipes, which are oriented perpendicularly to those visible in the L scans.

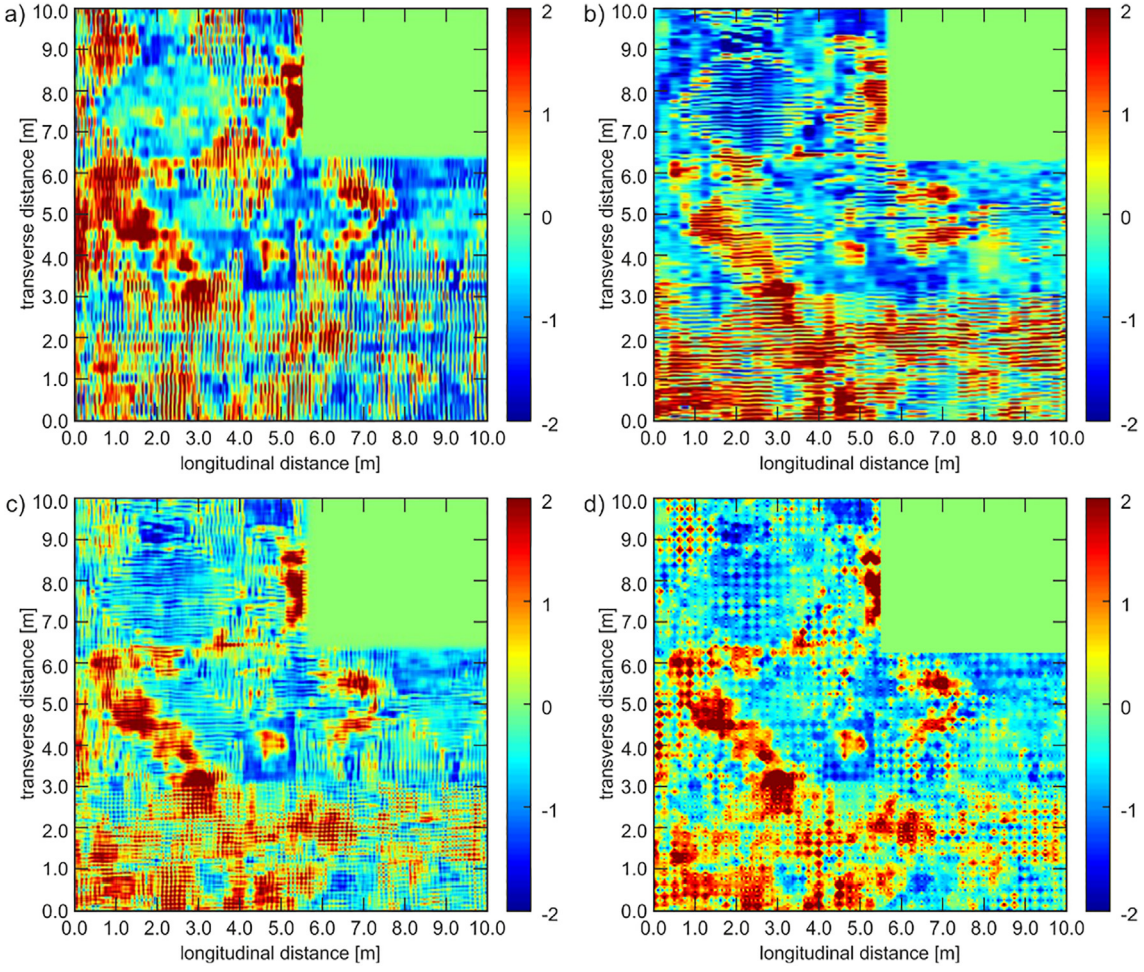

Fig. 8. GPR tomography maps for a depth of 7.50 cm (values in V): a) simple linear interpolation using longitudinal (L) scans, b) simple linear interpolation using transverse (T) scans, c) bilinear interpolation, d) IDW interpolation with a radius of 13 cm.

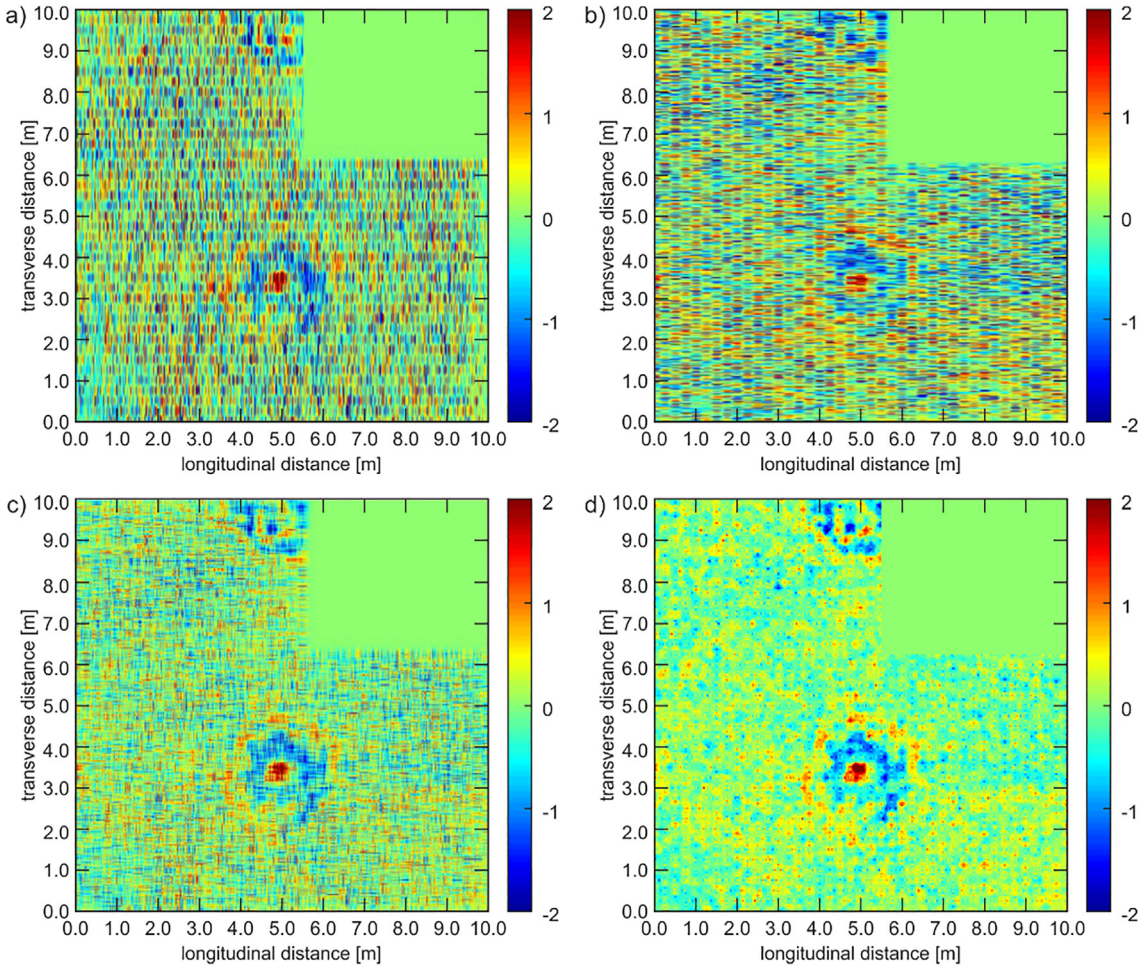

Fig. 9. GPR tomography maps for a depth of 132.5 cm (values in V): a) simple linear interpolation using longitudinal (L) scans, b) simple linear interpolation using transverse (T) scans, c) bilinear interpolation, d) IDW interpolation with a radius of 13 cm.

GPR tomography maps were prepared at depths of 4.6875 cm, 7.5 cm and 132.5 cm (Figs. 7–9, respectively). For each of these maps, the results obtained using the interpolation methods described in section 2.3 were compared: simple linear interpolation with longitudinal (a) and transverse (b) scans, bilinear interpolation using both scans (c) and IDW interpolation (d) for radius equal to 13 cm, which is the minimum value that ensures that the tomographic image will be complete. The C-scan at a depth of 4.6875 cm (Fig. 7) clearly indicates an area at the bottom of the map, where the reinforcing mesh was applied. The mesh is present neither in the remaining fragment of the tested floor nor near the entrance to the crypts. At a depth of approximately 7.5 cm (Fig. 8), the underfloor heating pipes were revealed at the upper part of the map. The exact course of individual loops can be observed. The visualisation of the pipes at the bottom part of the map was not possible due to multiple reflections of waves caused by the reinforcement mesh located above. C-scans at a depth of 132.5 cm (Fig. 9) indicated the location of the two entrances to the crypts. The visualised elements are probably foundations mentioned during the analysis of the GPR radargrams. One of the entrances is clearly marked in the centre of the map, at a distance of 5 m along the L axis and 3.5 m along the T axis. A second entrance appears at a distance of 5 m along the L axis, near the top edge of the map. These observations are consistent with the excavation view (Fig. 3b).

Comparing the interpolation methods applied, it can be concluded that, for elements with a linear course, such as underfloor heating pipes or reinforcing mesh, the best results were obtained by means of the bilinear interpolation that used both the longitudinal and transverse scans. For the volume anomalies (here: foundations under the entrances to the crypts) the IDW technique gave better results. Using this method allowed the basket effect to be reduced, which appeared in the bilinear interpolation (Fig. 9c).

3.2. GPR surveys of selected squares

The verification of the proposed interpolation methods with a scanning distance of 25 cm was conducted in three selected square sub-areas (denoted as S1, S2 and S3 in Fig. 3a) profiled additionally at a denser spacing (1 cm). The route, along which the antenna was moved, was drawn on a piece of paper. Longitudinal (L1-L26) and transversal (T27-T51) lines with start and end points of the antenna were marked on this route (Fig. 3c). The paper was placed on the floor at the locations marked as S1, S2 and S3 in Fig. 3a. The grid prepared in this way enabled a precise collection of scans at a constant distance of 1 cm (the axis marker traced each of the drawn lines during the measurements).

Figs. 10 and 11 depict maps obtained at depths of 4.6875 cm and 7.5 cm, respectively. At these depths, the reinforcing mesh and the floor heating system were detected. In Figs. 10 and 11, each column presents the results for each of the sub-areas, S1, S2 and S3, respectively. The first four rows (a-d) are fragments cut out of the original maps presented in Figs. 7 and 8, and they present results obtained by interpolation of the edge values at 25 cm spacing.

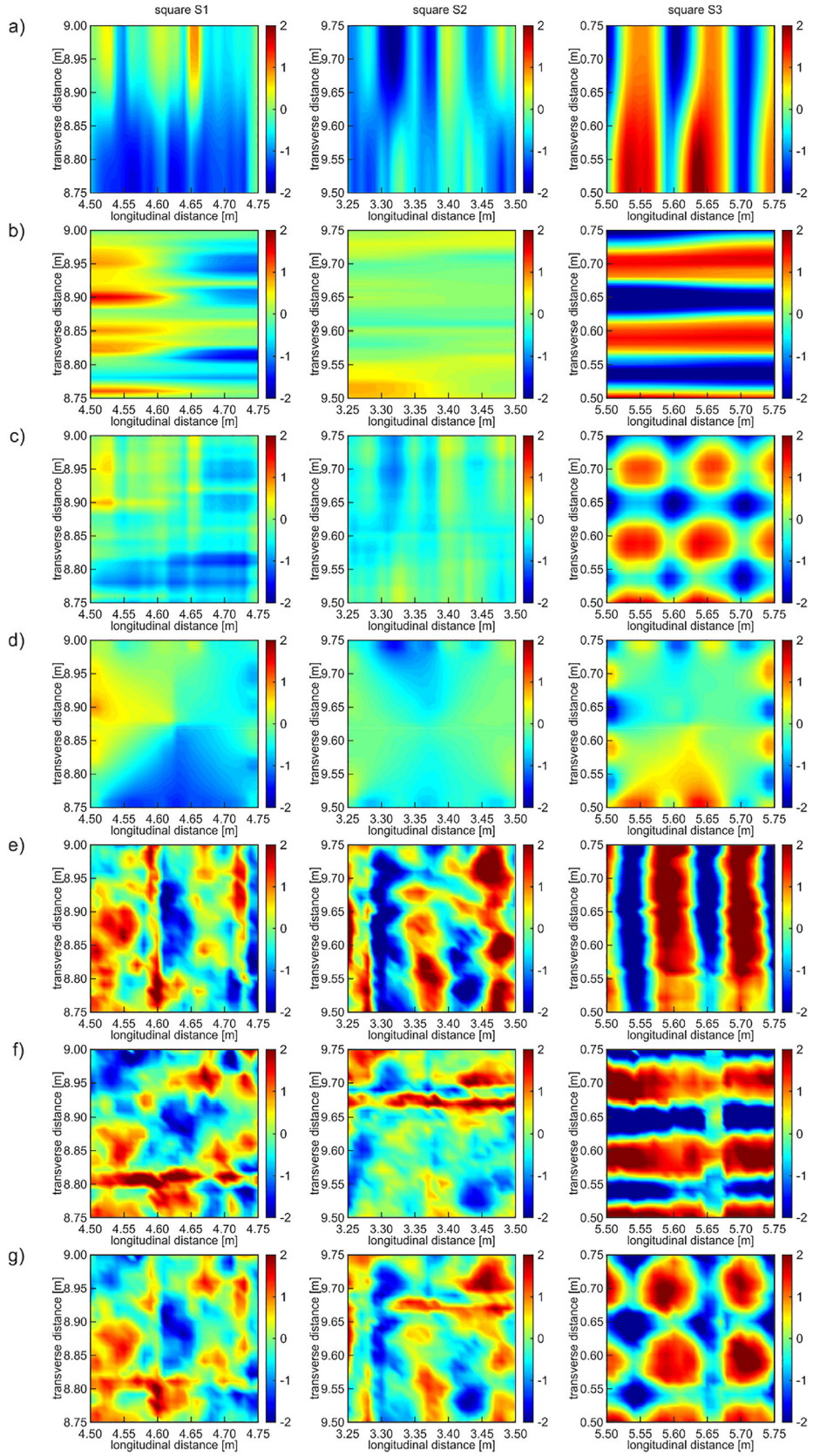

Fig. 10. GPR tomography maps for sub-areas S1, S2 and S3 at depth of 4.6875 cm (values in V): a) simple linear interpolation with L-scans (profile distance 25 cm), b) simple linear interpolation with T-scans (profile distance 25 cm), c) bilinear interpolation (profile distance 25 cm), d) IDW interpolation with a radius of 13 cm (profile distance 25 cm), e) exact image using L-scans (profile distance 1 cm), f) exact image using T-scans (profile distance 1 cm), g) exact image using both L and T-scans (profile distance 1 cm).

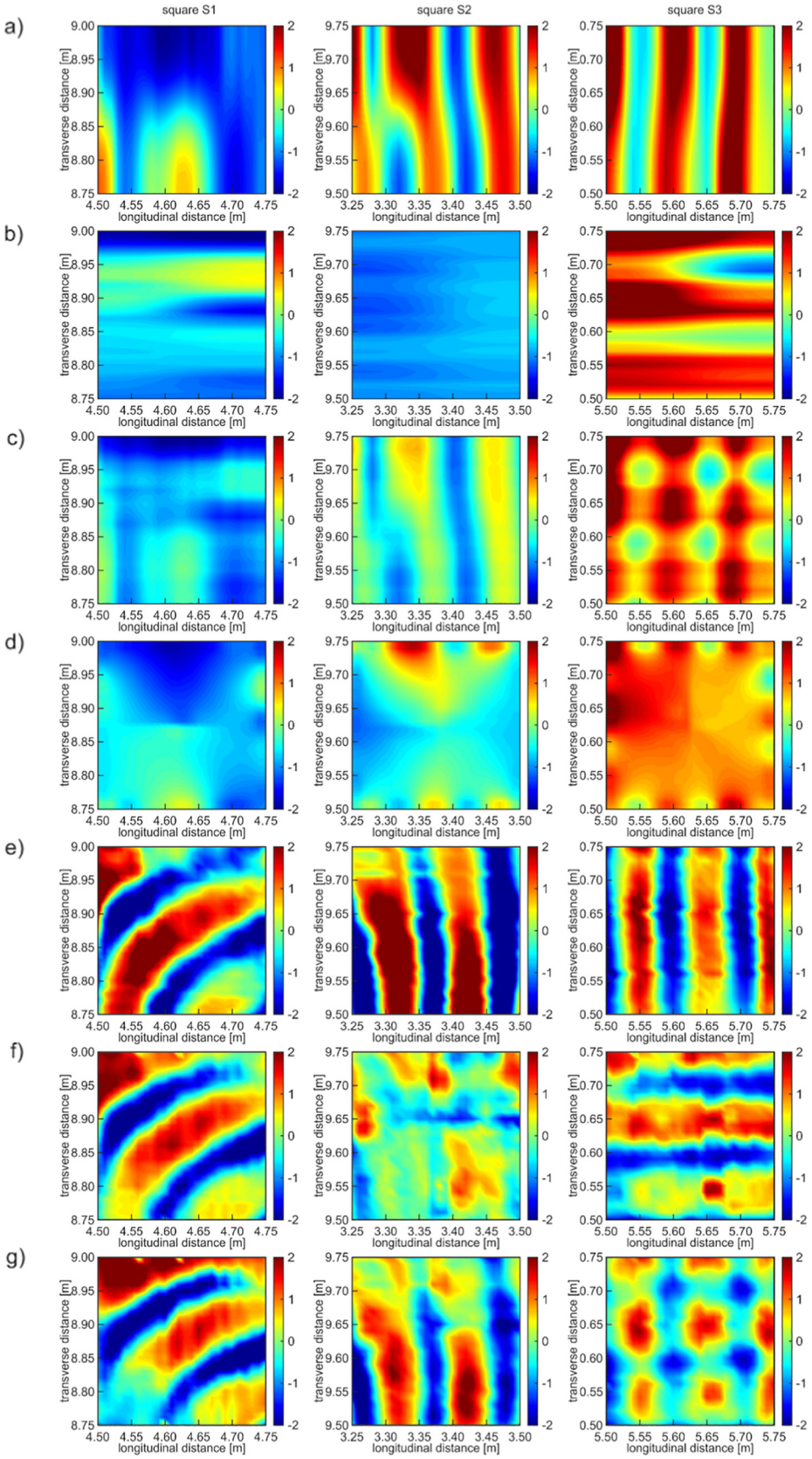

Fig. 11. GPR tomography maps for sub-areas S1, S2 and S3 at depth of 7.5 cm (values in V): a) simple linear interpolation with L-scans (profile distance 25 cm), b) simple linear interpolation with T-scans (profile distance 25 cm), c) bilinear interpolation (profile distance 25 cm), d) IDW interpolation with a radius of 13 cm (profile distance 25 cm), e) exact image using L-scans (profile distance 1 cm), f) exact image using T-scans (profile distance 1 cm), g) exact image using both L and T-scans (profile distance 1 cm).

The remaining three rows illustrate the maps prepared from the measurements without averaging, at a denser spacing of scans (i.e., 1 cm).

In Fig. 10, the reinforcing mesh is visible in square S3. The course of the reinforcing bars in both directions is most clearly visible on the maps prepared independently from the longitudinal and transverse scans (Fig. 10a, b). Bilinear interpolation maps (Fig. 10c), combining scans in both directions, are not uniformly legible because the upper and lower parts of the steel mesh are located at different depths and a perfect visualisation of the mesh at a single depth was not possible. The IDW interpolation (Fig. 10d) blurs the image of the mesh; therefore, it is useless in the analysed case. The simple linear and bilinear interpolation maps (Fig. 10a–c) agree well with maps prepared from the denser scan profiling (Fig. 10e–g).

Fig. 11 shows C-scans for a depth of 7.5 cm. The corner of the underfloor heating loop is visible in the S1 square. The heating pipes run partially in both the longitudinal and transverse directions, which is clearly visible in both the individual simple linear interpolation maps (Fig. 11a, b). The corner is also visible when both directions are combined (Fig. 11c). The IDW technique (Fig. 11d) again gave inadequate results. The S2 square illustrates the vertical direction of the floor heating pipes (with a slight bend in the upper part). The unidirectional course is visible on the maps from longitudinal and two-dimensional scanning (Fig. 11a, c). However, it was impossible to detect the pipes in the transverse direction (Fig. 11b). IDW interpolation also provided an incorrect result (Fig. 11d). The main conclusion is that the efficiency of the linear interpolation is less for curvilinear elements (such as corners or bends). In the S3 square, a reinforcing mesh is visible, although it was not placed at the depth of 7.5 cm. This is probably a consequence of additional reflections from the upper reinforcing mesh.

4. Conclusions

In this study, GPR investigations were conducted on the floor of a historical church. Experimental measurements and specific data processing techniques allowed tomographic maps of several specific underfloor elements to be obtained. The study supports the following conclusions.

- The interpretation of B-scans for particular longitudinal and transverse traces provided important information about the structure of the floor as well as buried structures under the floor. Radargrams revealed the existence of elements such as reinforcing bars, floor heating pipes and foundations under the entrances to the crypts and also showed their depth. Such an approach can be an initial step of analysis for collected data. To obtain more useful information, further signal processing is required.
- The tomographic imaging provided cross sections of the floor for particular depths. These images showed the location and orientation of structural elements in the horizontal plane. Preparation of tomographic maps from scans collected over wide spacing required additional calculations, such as the interpolation of unknown values between the known ones. Simple linear interpolation, bilinear interpolation and inverse distance weighting interpolation techniques can be successfully employed to improve tomographic maps.
- Despite their simplicity, methods based on linear interpolation can be successfully used for GPR tomographic imaging. The simple linear interpolation can detect linear patterns oriented perpendicular to the original direction of the scan traces. As a product of two simple interpolations, a bilinear variant enables detection of linear patterns in both directions. This method becomes less efficient when the direction of a tracked element changes (bends and corners, especially curved).
- The inverse distance weighting technique appeared to be ineffective for identifying linear and mesh structures. However, this approach can be successfully used to detect concentrated (volume) elements.

In summary, GPR tomographic imaging is an efficient method for inspecting the underfloor structures in cultural heritage buildings. However, the data collected requires further signal processing techniques to provide useful information.

CRediT authorship contribution statement

Magdalena Rucka: Conceptualization, Methodology, Formal analysis, Writing - review & editing, Supervision. **Erwin Wojtczak:** Methodology, Software, Investigation, Writing - original draft, Visualization. **Monika Zielińska:** Methodology, Software, Investigation, Writing - original draft, Visualization.

Declaration of Competing Interest

The authors declare that they have no known competing financial interests or personal relationships that could have appeared to influence the work reported in this paper.

Acknowledgments

The authors would like to thank the Missionary Oblates of Mary Immaculate for contributing photographs of the floor in St. Joseph's Church in Gdańsk from the renovation (the photographs were used in Fig. 1). The help of Patryk Muntowski, who provided a photogrammetric map of the crypts, is also gratefully acknowledged (the map was used in the background of Fig. 3b).

References

[1] C. Brooke, Thermal Imaging for the Archaeological Investigation of Historic Buildings, Remote Sens. 10 (2018) 1401, https://doi.org/10.3390/rs10091401.
[2] E. Alexakis, E.T. Delegou, K.C. Lampropoulos, M. Apostolopoulou, I. Ntoutsi, A. Moropoulou, NDT as a monitoring tool of the works progress and the assessment of materials and rehabilitation interventions at the Holy Aedicule of the Holy Sepulchre, Constr. Build. Mater. 189 (2018) 512–526, https://doi.org/10.1016/j.conbuildmat.2018.09.007.
[3] M.I. Martínez-Garrido, R. Fort, M. Gómez-Heras, J. Valles-Iriso, M.J. Varas-Muriel, A comprehensive study for moisture control in cultural heritage using non-destructive techniques, J. Appl. Geophys. 155 (2018) 36–52, https://doi.org/10.1016/j.jappgeo.2018.03.008.
[4] L. Courard, A. Gillard, A. Darimont, J.M. Bleus, P. Paquet, Pathologies of concrete in Saint-Vincent Neo-Byzantine Church and Pauchot reinforced artificial stone, Constr. Build. Mater. 34 (2012) 201–210, https://doi.org/10.1016/j.conbuildmat.2012.02.070.
[5] P. Lopez-Arce, M. Tagnit-Hammou, B. Menendez, J.D. Mertz, M. Guiavarc'h, A. Kaci, S. Aggoun, A. Cousture, Physico-chemical stone-mortar compatibility of commercial stone-repair mortars of historic buildings from Paris, Constr. Build. Mater. 124 (2016) 424–441, https://doi.org/10.1016/j.conbuildmat.2016.07.076.
[6] B. Jonaitis, V. Antonovič, A. Šneideris, R. Boris, R. Zavalis, Analysis of Physical and Mechanical Properties of the Mortar in the Historic Retaining Wall of the Gediminas Castle Hill (Vilnius, Lithuania), Materials (Basel). 12 (2018) 8, https://doi.org/10.3390/ma12010008.
[7] Y. Boffill, H. Blanco, I. Lombillo, L. Villegas, Assessment of historic brickwork under compression and comparison with available equations, Constr. Build. Mater. 207 (2019) 258–272, https://doi.org/10.1016/j.conbuildmat.2019.02.083.
[8] D.M. McCann, M.C. Forde, Review of NDT methods in the assessment of concrete and masonry structures, NDT E Int. 34 (2001) 71–84, https://doi.org/10.1016/S0963-8695(00)00032-3.
[9] A.C. Kak, M. Slaney, Principles of Computerized Tomographic Imaging, The Institiute of Electrical and Electronics Engineers Inc, New York, 1988.
[10] L. Binda, A. Saisi, C. Tiraboschi, S. Valle, C. Colla, M. Forde, Application of sonic and radar tests on the piers and walls of the Cathedral of Noto, Constr. Build. Mater. 17 (2003) 613–627, https://doi.org/10.1016/S0950-0618(03)00056-4.
[11] V. Pérez-Gracia, J.O. Caselles, J. Clapés, G. Martinez, R. Osorio, Non-destructive analysis in cultural heritage buildings: Evaluating the Mallorca cathedral

supporting structures, NDT E Int. 59 (2013) 40–47, https://doi.org/10.1016/j.ndteint.2013.04.014.
[12] E. Zendri, L. Falchi, F.C. Izzo, Z.M. Morabito, G. Driussi, A review of common NDTs in the monitoring and preservation of historical architectural surfaces, Int. J. Archit. Herit. 11 (2017) 987–1004, https://doi.org/10.1080/15583058.2017.1331477.
[13] M. Zielińska, M. Rucka, Non-Destructive Assessment of Masonry Pillars using Ultrasonic Tomography, Materials (Basel). 11 (2018) 2543, https://doi.org/10.3390/ma11122543.
[14] T. Shiotani, S. Momoki, H. Chai, D.G. Aggelis, Elastic wave validation of large concrete structures repaired by means of cement grouting, Constr. Build. Mater. 23 (2009) 2647–2652, https://doi.org/10.1016/j.conbuildmat.2009.01.005.
[15] H.K. Chai, K.F. Liu, A. Behnia, K. Yoshikazu, T. Shiotani, Development of a tomography technique for assessment of the material condition of concrete using optimized elastic wave parameters, Materials (Basel). 9 (2016) 291, https://doi.org/10.3390/ma9040291.
[16] V.G. Haach, F.C. Ramirez, Qualitative assessment of concrete by ultrasound tomography, Constr. Build. Mater. 119 (2016) 61–70, https://doi.org/10.1016/j.conbuildmat.2016.05.056.
[17] Ł. Drobiec, R. Jasiński, W. Mazur, Accuracy of eddy-current and radar methods used in reinforcement detection, Materials (Basel) 12 (2019) 1168, https://doi.org/10.3390/ma12071168.
[18] K. Schabowicz, Ultrasonic tomography – The latest nondestructive technique for testing concrete members - Description, test methodology, application example, Arch. Civ. Mech. Eng. 14 (2014) 295–303, https://doi.org/10.1016/j.acme.2013.10.006.
[19] W. Neubauer, A. Eder-Hinterleitner, S. Seren, P. Melichar, Georadar in the Roman civil town Carnuntum, Austria: An approach for archaeological interpretation of GPR data, Archaeol. Prospect. 9 (2002) 135–156, https://doi.org/10.1002/arp.183.
[20] D. Goodman, Y. Nishimura, J.D. Rogers, GPR time slices in archaeological prospection, Archaeol. Prospect. 2 (1995) 85–89.
[21] L. Orlando, Georadar data collection, anomaly shapeand archaeological interpretation – a case study from central Italy, Archaeol. Prospect. 14 (2007) 213–225, https://doi.org/10.1002/arp.311 Georadar.
[22] G. De Donno, L. Di Giambattista, L. Orlando, High-resolution investigation of masonry samples through GPR and electrical resistivity tomography, Constr. Build. Mater. 154 (2017) 1234–1249, https://doi.org/10.1016/j.conbuildmat.2017.06.112.
[23] R. Samet, E. Çelik, S. Tural, E. Şengönül, M. Özkan, E. Damcı, Using interpolation techniques to determine the optimal profile interval in ground-penetrating radar applications, J. Appl. Geophys. 140 (2017) 154–167, https://doi.org/10.1016/j.jappgeo.2017.04.003.
[24] P. Klęsk, M. Kapruziak, B. Olech, Statistical moments calculated via integral images in application to landmine detection from Ground Penetrating Radar 3D scans, Pattern Anal. Appl. 21 (2018) 671–684, https://doi.org/10.1007/s10044-016-0592-5.
[25] W. Zhao, E. Forte, F. Fontana, M. Pipan, G. Tian, GPR imaging and characterization of ancient Roman ruins in the Aquileia Archaeological Park, NE Italy, Meas. J. Int. Meas. Confed. 113 (2018) 161–171, https://doi.org/10.1016/j.measurement.2017.09.004.
[26] D. Shepard, Two-dimensional interpolation function for irregularly- spaced data, in: Proc. – 1968 ACM Natl. Conf., 1968: pp. 517–524
[27] F.W. Chen, C.W. Liu, Estimation of the spatial rainfall distribution using inverse distance weighting (IDW) in the middle of Taiwan, Paddy Water Environ. 10 (2012) 209–222, https://doi.org/10.1007/s10333-012-0319-1.
[28] Y. Mito, M.A.M. Ismail, T. Yamamoto, Multidimensional scaling and inverse distance weighting transform for image processing of hydrogeological structure in rock mass, J. Hydrol. 411 (2011) 25–36, https://doi.org/10.1016/j.jhydrol.2011.09.018.
[29] M. Jing, J. Wu, Fast image interpolation using directional inverse distance weighting for real-time applications, Opt. Commun. 286 (2013) 111–116, https://doi.org/10.1016/j.optcom.2012.09.011.
[30] D. Goodman, S. Piro, GPR remote sensing in archaeology, 2013. doi:10.1007/978-3-642-31857-3.
[31] L. De Mesnard, Computers & geosciences pollution models and inverse distance weighting : some critical remarks, Comput. Geosci. 52 (2013) 459–469, https://doi.org/10.1016/j.cageo.2012.11.002.